Article

MOF-Based Materials with Sensing Potential: Pyrrolidine-Fused Chlorin at UiO-66(Hf) for Enhanced NO$_2$ Detection

Carla Queirós [1], Francisco G. Moscoso [2], José Almeida [1], Ana M. G. Silva [1], Ahmad Sousaraei [3], Juan Cabanillas-González [3], Manuela Ribeiro Carrott [4], Tânia Lopes-Costa [2], José M. Pedrosa [2,*] and Luís Cunha-Silva [1,*]

[1] LAQV-REQUIMTE, Department of Chemistry and Biochemistry, Faculty of Sciences, University of Porto, 4169-007 Porto, Portugal
[2] Department of Physical, Chemical and Natural Systems, University Pablo de Olavide, Ctra. Utrera Km. 1, 41013 Sevilla, Spain
[3] Madrid Institute for Advanced Studies in Nanoscience, IMDEA Nanociencia, Universitaria de Cantoblanco, Calle Faraday 9, 28049 Madrid, Spain
[4] LAQV-REQUIMTE, Institute for Research and Advanced Studies, Department of Chemistry and Biochemistry, School of Sciences and Technology, University of Évora, 7000-671 Évora, Portugal
* Correspondence: jmpedpoy@upo.es (J.M.P.); l.cunha.silva@fc.up.pt (L.C.-S.)

Abstract: An efficient strategy to develop porous materials with potential for NO$_2$ sensing was based in the preparation of a metal-organic framework (MOF), UiO-66(Hf), modified with a very small amount of *meso*-tetrakis(4-carboxyphenyl) *N*-methylpyrrolidine-fused chlorin (TCPC), TCPC@MOF. Chlorin's incorporation into the UiO-66(Hf) framework was verified by several characterization methods and revealed that the *as*-synthesized TCPC@MOF brings together the chemical stability of UiO-66(Hf) and the photophysical properties of the pyrrolidine-fused chlorin which is about five times more emissive than the porphyrin counterpart. TCPC@MOF was further incorporated into polydimethylsiloxane (PDMS) and the resulting TCPC@MOF@PDMS film was tested in NO$_2$ gas sensing. It showed notable sensitivity as well as a fast response in the range between 0.5 and 500 ppm where an emission intensity quenching is observed up to 96% for 500 ppm. This is a rare example of a chlorin-derivative used for gas-sensing applications through emission changes, and an unusual case of this type of optical-sensing composites of NO$_2$.

Keywords: *N*-methylpyrrolidine-fused chlorin; metal-organic framework; composite; optical sensor; NO$_2$ sensing

1. Introduction

Air pollution remains a major health concern worldwide. According to the 2021 Air Quality Status briefing by the European Environment Agency, many European cities still regularly exceed current Union's emission limits for air pollutants [1]. Nitrogen oxides (NO$_x$) belong to one category of these air pollutants, and nitrogen dioxide (NO$_2$) is the most toxic and prevalent form of the NO$_x$ family. NO$_2$ is a nose and throat irritant that can cause serious respiratory problems [2], reduce respiratory defense mechanisms, and increase infection rates [3], and was related to 55,000 premature deaths in 2018 in Europe alone [4]. The early detection of NO$_2$ has also shown to be a great asset for fire detection and firefighting improvement [5]. Several colorimetric materials were shown to be quite efficient for the detection of CO and NO$_2$ gases produced in an early fire [6]. Given this scenario, the detection of toxic gases plays an increasingly important role in keeping our environment unpolluted and ourselves safe due to their dangerous effects on both the ecosystem and human health.

Nowadays there is a wide variety of gas-sensing devices based on different materials and operation mechanisms [7]. Some of those materials are based on metal-organic

frameworks (MOF), which are a category of porous coordination polymers assembled by the coordination of metal cationic centers with organic linkers. Given the wide range of available metal ions and organic linkers used in an MOF assembly, these materials have become increasingly attractive because of their wide-variety of topologies and broad-range of chemical and physical properties. Excellent literature reviews and in-depth studies have been reported regarding MOF applications as materials to capture and degrade toxic chemicals [8–13], as well as luminescent sensors [14–21], enzyme biomimetics [22,23], and catalysts [24,25]. One of the most studied and hydrothermal stable MOFs is the UiO-66(Zr) that consists of hexanuclear, octahedral zirconium(IV) oxo clusters connected through terephthalic acid linkers to form a 3D highly-porous rigid framework. This crystalline framework has shown resistance to a wide range of different solvents including strong acids and bases [26]. UiO-66(Zr) has been intensely studied as a fluorescent sensor in the past decade although terephthalic acid and consequently UiO-66(Zr) both possess low fluorescence intensities. Zirconium (Zr) MOFs are widely used; however, some characteristics of hafnium (Hf) MOFs, namely their acidic nature, mechanical and higher chemical stability, also make them promising materials for several applications [27,28]. Due to their same d^0 electronic configuration and identical ionic radius (78 pm), substituting Zr(IV) with Hf(IV) in the UiO-66 synthesis results in an MOF with the same topology of UiO-66(Zr) but with stronger acid sites. This property of UiO-66(Hf) was originally shown to have applications as a radiation scavenger [26] and contrast agent for computed tomography [29]. Nevertheless, there are few examples of UiO-66(Hf) as a sensor to detect free chlorine in waters [30], uric acid in biological fluids [31], and peroxynitrite in living cells [32].

A common strategy to endow the MOF with fluorescent properties is to dope it with a lanthanide ion or to integrate (impregnate or incorporate) a fluorophore (such as rhodamine or porphyrin derivatives) into the MOF structure [33–38], creating a luminescent MOF. This strategy allows an optimization of several properties and broadens their application [39,40]. Luminescent MOF sensor characteristics/properties make them stand out in comparison with other luminescent sensors [40–42], namely: (i) their porosity allows the adsorption and pre-concentration of the analytes, increasing the host-guest interactions; (ii) they can be easily functionalized and therefore more tunable to sense specific analytes; (iii) they produce guest-dependent optical signals usually translated into vaporchromic or solvatochromic responses; (iv) they make it possible to study the sensing mechanisms at the molecular level due to their crystalline nature; (v) they possess stability in water even at the basic range; and (vi) they can be used to prepare composites/hybrids that combine their advantages with those of other compounds/materials.

One of the major advantages of incorporating fluorescent ligands into MOFs is to prevent their aggregation and consequently their self-quenching. This can be attained since MOFs open structures allow the separation of the fluorescent unit by relatively large distances (>5 Å), while maintaining or even amplifying the sensing signals upon interaction with analytes. The signal amplification can occur due to the existence of an efficient energy migration (exciton hoping) along the composite, similar to that of conjugated polymers, even when only a few analyte molecules interact with the composite [40]. Nevertheless, working with powder materials may be challenging and their immobilization in solid matrices like TiO_2, PDMS (polydimethylsiloxane) or PMMA (poly(methyl methacrylate)) can improve the molecular recognition of analytes. These composites are also, in general, property-tunable and possess better resistance to degradation and better flexibility, among other advantageous properties [43]. This type of composite is immensely appealing when the analytes are gases or volatile organic compounds (VOC) [42].

Porphyrins are very interesting fluorophores that can be incorporated into MOF frameworks, either via chemical bonds or non-covalently [44,45]. The integration of porphyrins in MOFs was shown to be advantageous to obtain multifunctional drug carriers [46], as well as biomaterials [47]. A tremendous number of MOFs have been used as a host for the porphyrin's incorporation, providing efficient platforms to encapsulate and deliver pharmaceuticals, imaging agents, and enzymes [45,48]. Reduced porphyrins (7,8-dihydroporphyrins,

also known as chlorins; Figure 1a–d,f) are much more interesting chromo- and fluorophores for integrating into MOFs due to the enhanced absorbance of the QI (0-0) band centered at 650 nm and high fluorescence quantum yield at the same region. The incorporation of chlorins into MOF materials has been predominantly studied in the area of photodynamic therapy (PDT) of cancer, where chlorin e6 (Figure 1a) stands out as the photosensitizer of choice [49–52]. On the other hand, *N*-methylpyrrolidine-fused chlorins are more stable than the hydrogenated chlorins and have been studied mostly as photosensitizers in the photodynamic inactivation of bacteria [53–55] and PDT of cancer [56–59], as well as reaction [60], biomimetic [61], and oxidation [62] catalysts.

In the last years, our research group has been developing optical sensors for NO$_2$ including: (i) rosamine-based composite film sensors, immobilized on SiO$_2$ [63] and TiO$_2$ [64]; and (ii) a Tb(BTC) MOF material (BTC: benzene-1,3,5-tricarboxylate) embedded into transparent polymeric matrices to produce mixed-matrix membranes [65–68]. In 2021, the first use of an *N*-methylpyrrolidine-fused chlorin in an MOF was reported by Sakamaki et al. for PDT application [69]. Meanwhile, we recently reported the first sensing application of *N*-methylpyrrolidine-fused 5,10,15,20-tetrakis(4-carboxyphenyl)chlorin (TCPC, Figure 1f), anchored to a nanostructured porous TiO$_2$ substrate, as a fluorescent sensor of the explosive triacetone triperoxide (TATP) in the gas phase [70]. Following our interest in the study and application of MOF-based materials for sensing [65–68], the pyrrolidine-fused chlorin (TCPC) was incorporated into UiO-66(Hf) by a one-pot solvothermal synthesis (TCPC@MOF) and this material was characterized in the solid state, using several techniques. For comparison purposes, a porphyrinic material (TCPP@MOF) was further prepared and characterized. Then, TCPC@MOF was embedded into a polydimethylsiloxane (PDMS) matrix and used in the optical detection of NO$_2$ gas, revealing good sensitivity. This work is one of the few examples of a chlorin@MOF composite used in optical gas sensing, particularly using fluorescence spectroscopy. In general, porphyrin derivatives are the selected sensing probes [71–73] and the detection "mechanism" is based on the chemiresistive or semiconducting nature of the materials/composites [74–76].
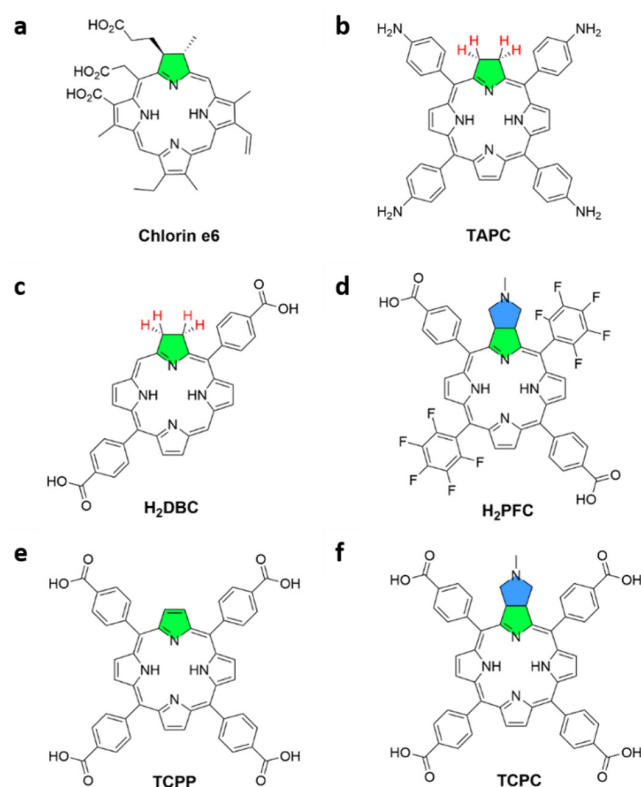

Figure 1. Structures (**a**–**d**) are some examples of porphyrins and chlorins previously reported for

their inclusion in MOF materials: (**a**) chlorin e6 [49–52]; (**b**) TAPC (*meso*-tetrakis(4-aminophenyl)chlorin) [77]; (**c**) H_2DBC (5,15-bis(4-carboxylphenyl)chlorin) [78]; and (**d**) H_2PFC (5,15-bis(4-carboxylphenyl)-10,20-bis(pentafluorophenyl)chlorin) [69]. Structures (**e**,**f**) represent those used in this work: (**e**) TCPP (*meso*-tetrakis(4-carboxyphenyl)porphyrin) and (**f**) TCPC (*meso*-tetrakis(4-carboxyphenyl) *N*-methylpyrrolidine-fused chlorin) [70].

2. Materials and Methods

2.1. Chemicals and Instruments

Benzene-1,4-dicarboxylic acid (terephthalic acid or H_2BDC) 98%, sodium hydroxide (NaOH) >98%, *meso*-tetrakis(4-carboxyphenyl)porphyrin (TCPP) dye content 75%, and anhydrous *N*,*N*-dimethylformamide (DMF) 99.8% were purchased from Sigma-Aldrich. Hafnium (IV) chloride ($HfCl_4$, metal basis) Zr < 0.5%, 99.9%, was obtained from Alfa Aesar. Formic acid 98/100% (analytical reagent grade), ethanol (analytical reagent grade) $\geq$99.9%, methanol (analytical reagent grade) $\geq$99.9%, dichloromethane (analytical reagent grade) $\geq$99.8%, and tetrahydrofuran (analytical reagent grade) were supplied by Fisher. Chloridric acid (HCl) 37% and sodium chloride (NaCl) were purchased from VWR Chemicals. Polydimethylsiloxane (Sylgard 184) was supplied by Dow Corning. All these chemicals were purchased as solvent or reagent-grade and used without further purification, unless otherwise stated. Flash chromatography was carried out using silica gel (Merck, 230–400 mesh). The amount of TCPP and TCPC present in UiO-66(Hf) was assessed by UV-Vis (at the corresponding $\lambda_{abs\,max}$), using calibration curves determined for TCPP and TCPC in DMF. Room temperature PXRD patterns were collected at The Institute of Physics for Advanced Materials, Nanotechnology and Photonics (IFIMUP) using a Rigaku SmartLab diffractometer (Cu Kα1,2 radiation, λ_1 = 1.540593 Å and λ_2 = 1.544414 Å) using: zero-background sample holder; 200 mA and 45 kV in a Bragg−Brentano para-focusing optics configuration; a D/teX Ultra 250 silicon strip detector; step counting method (step: 0.01°) in continuous mode; $3.0° \leq 2\theta \leq 50°$ range. FT-IR spectra were obtained neat with a FT-IR Perkin Elmer Spectrum BX with an attenuated total reflectance (ATR) used for acquiring FT-IR spectra (range: $400-4000$ cm^{-1}). Scanning electron microscope (SEM) images were acquired at the Materials Centre of the University of Porto (CEMUP) using a FEI Quanta 400FEG ESEM/EDAX Genesis X4M (15 keV). Thermogravimetric Analysis (TGA) was performed at FCUP|DQB Lab&Services using a Hitachi (STA7200RV) thermal analyzer (Hitachi, Japan) with a ramp of 5 °C/min under nitrogen (200 mL/min) from 30 to 600 °C. Shimadzu-UV 3600 UV-Vis-NIR spectrophotometer was used to record electronic absorption spectra, and emission spectra were recorded with a Varian Cary Eclipse spectrofluorometer (Agilent Technologies, Sta Clara, CA, USA), using 5 nm slits width. All measurements were performed at 25 °C and the absorbance's sample values were kept below 0.1. Stock solutions of TCPP, TCPC, and suspensions of the MOFs (UiO-66(Hf), TCPP@MOF and TCPC@MOF) were prepared in DMSO. The DMSO stock solution/suspension was diluted to the required final concentration in the different solvents. Zeta potentials were obtained on a Malvern Zetasizer Nano using suspensions of the MOFs in milli-Q water and ethanol, and solutions of the ligands in ethanol, at 25 °C. Approximately 1 mg of the compounds (ligands and materials) was dispersed in 3 mL of ethanol or milli-Q water and sonicated 5 min prior to the measurement. The measurements were performed in triplicate, at 25 °C. N_2 adsorption-desorption isotherms were determined at -196 °C on a Quantachrome Quadrasorb equipped with a turbomolecular pump, using helium and nitrogen of 99.999% purity. Prior to the measurements, the samples were outgassed, under turbomolecular pump vacuum, for 8 h at 80 °C using a heating rate of 1 °C min^{-1}, and afterwards for further 12 h at 120 °C, with a heating rate of 2 °C min^{-1} to achieve this temperature. Photoluminescence (PL) and excitation spectra of TCPC/TCPP@MOF@PDMS films were recorded with a Hitachi F-7000 fluorescence spectrophotometer (Hitachi, Japan). Additionally, the absorption spectra of the membranes were obtained after each FL measurement using an Agilent Cary 100 UV-Vis spectrophotometer (Agilent Technologies, Sta Clara, CA, USA). Scanning electron microscopy (SEM) images of the films were obtained at 5 kV using an

FEI Teneo microscope. X-Ray diffraction (XRD) pattern of the membranes were collected using a Discover D8 (Bruker) diffractometer in a with Cu Kα radiation (1.5406 Å, 50 kV, 1000 mA) in the range from 5° to 35° 2θ with a step of 0.02° *per* 0.5 s.

2.2. Synthesis

TCPC was synthesized from the 1,3-dipolar cycloaddition of *meso*-tetrakis(4-methoxy-carbonylphenyl)porphyrin with azomethine ylide, and subsequent hydrolysis of the methyl ester, following the procedure described in literature [70]. The MOFs were prepared according to the literature with slight variations [79,80].

UiO-66(Hf). The solvothermal synthesis of UiO-66(Hf) was done based on one-pot solvothermal reaction reported in the literature [79]. A mixture of H_2BDC (42.3 mg, 0.25 mmol, 1.00 equiv.) and $HfCl_4$ (82.1 mg, 0.26 mmol, 1.01 equiv.) was dissolved in a solvent mixture (9:1, *v/v*, 10 mL) of *N,N*-dimethylformamide (DMF)/formic acid. Then the mixture was transferred into a Teflon-lined autoclave and heated at 123 °C for 40 h. The product was centrifuged (12.000 rpm, 3 min) and soaked in methanol for 2 h at room temperature under stirring. After this time, the material was centrifuged and soaked in dichloromethane for 2 h. The solid was recovered by centrifugation and dried under vacuum (50 mbar) at 120 °C for 24 h (99 mg).

TCPC@MOF. This material was prepared by adapting the protocol existent in the literature [80]. Briefly, we mixed 50 mg of H_2BDC (0.30 mmol, 1.0 equiv.), 117 mg of $HfCl_4$ (0.37 mmol, 1.2 equiv.), and 8.4 mg of TCPC (10 μmol, 0.03 equiv.) in a 13 mL glass vial containing 10 mL of anhydrous DMF. After 5 min of magnetic stirring, the mixture was heated at 120 °C for 24 h under solvothermal conditions (Teflon-lined reactor sealed in a stainless-steel vessel). A reddish solid was collected by centrifugation (12.000 rpm, 2 min), washed several times using DMF, methanol and THF, and ultimately dried under vacuum (50 mbar) at 120 °C for 24 h; 134 mg.

TCPP@MOF. This material was prepared in the same manner as TCPC@MOF, with slight variations. The material was prepared in a glass vial (13 mL) using a mixture of H_2BDC (51 mg, 0.31 mmol, 1.0 equiv.), $HfCl_4$ (114 mg, 0.36 mmol, 1.2 equiv.), and TCPP (8.8 mg, 11.1 μmol, 0.04 equiv.) in anhydrous DMF (10 mL). After 5 min of stirring the mixture was heated under solvothermal conditions at 120 °C for 24 h. The brownish solid was collected by centrifugation, washed several times using DMF and methanol, and dried under vacuum at 120 °C for 24 h; 133 mg.

2.3. Film Preparation

Sylgard® 184 base and curing agent were combined in a 10:1 weight ratio (1 g and 0.1 g, respectively) and were vigorously stirred for 30 min. Then, 15 mg of TCPC@MOF material was poured into the mixture under magnetic stirring until a complete dispersion of the powder was reached. Next, the mixture was spin-coated on a petri dish at 1000 rpm for 60 s and then placed in an oven at 60 °C overnight. Finally, the TCPC@UiO-66@PDMS were cut and peeled off on demand.

2.4. Time-Resolved Photoluminescence (PL) Measurements

Photoluminescence lifetime measurements were carried out with the technique of time-correlated single photon counting. The PL was excited with a PDL 828 Picoquant Sepia diode laser delivering 50 ps pulses at 405 nm at a 10 MHz repetition rate. The photoluminescence was collected in free-space and focused onto the slit of a SP2500, Acton Research 1/2 m spectrometer. A Picoquant PMA Hybrid-Photomultiplier Assembly with a transit time spread of less than 50 ps was employed as detector. Nanosecond PL decays were recorded with a Picoquant Hydraharp time-correlated single-photon counting (TCSPC) electronics. PL decay curves, deconvoluted from the instrumental response function, were fitted to multi-exponential laws using Picoquant Fluofit analysis software which provided individual decay components with their corresponding statistical weight as well as amplitude-averaged PL decay values.

2.5. NO$_2$ Sensing Studies

For the sensing experiments, TCPC@MOF@PDMS films were placed into a purpose-built gas chamber made with a 3-D printer, using polylactic acid (PLA) filaments. A gas inlet and outlet, as well as two quartz windows compatible with the spectrophotometer, were also mounted on the chamber. Two Bronkhorst$^®$ F-201FV mass flow controllers were used to regulate the gas flow rates. A steady flow of dry N$_2$ was kept during the sample handling to avoid contamination. Different NO$_2$ concentrations were obtained from 500, 50 and 5 ppm cylinders and their subsequent dilution with N$_2$. The gas flow rate entering the chamber was fixed at 1 L·min^{-1} in all cases. Once the toxic gas was introduced into the chamber, the fluorescence (FL) was recorded until the complete saturation of the sample was reached.

3. Results and Discussion

3.1. MOF-Based Materials

The incorporation of the chlorin and porphyrin molecules into the UiO-66(Hf) framework was performed by using a one-pot solvothermal reaction, with a proportion in mass of TCPC and TCPP relative to the total reactants mass of only 0.03 and 0.04, respectively. The TCPC@MOF and TCPP@MOF materials were afforded in similar yield and the content of TCPC and TCPP in the MOFs was determined as being 1.8% of TCPC and 2.0% of TCPP, for TCPC@MOF and TCPP@MOF, respectively (more details about the content determination in Supplementary Information, Section S1). An initial indication of the successful material preparation was the color change from white, correspondent to UiO-66(Hf) (MOF), to the brownish and reddish coloration of TCPC@MOF and TCPP@MOF, respectively (Figure 2a). This color was retained after several washings with DMF and methanol (plus THF for TCPC@MOF). The extent of the porphyrin derivatives incorporation (coordination) in the MOFs' matrix, or impregnation at the pores of UiO-66(Hf) framework, is a complex process that demands an extended characterization of materials, including PXRD, SEM-EDS, FT-IR, DLS, and zeta potential.

The successful preparation of crystalline UiO-66(Hf) and corresponding TCPP and TCPC MOFs was initially verified by PXRD analysis. The similarity in the Bragg diffraction peaks validates that the UiO-66-typed topology is retained after the one-pot reaction with TCPC and TCPP (Figure 2b), in particular by the unequivocal observation of the two main peaks associated with the (111) reflection [26]. Nevertheless, the diffraction patterns reveal some loss of crystallinity for TCPC@MOF and TCPP@MOF, most probably suggesting some interaction in the UiO-66(Hf) structure with TCPC and TCPP. In terms of morphology and composition, the materials were further studied by SEM-EDS (Figure 2c–e), revealing the expected regular polyhedral particles for UiO-66(Hf) [81] and more irregular particle agglomerates for TCPC@MOF and TCPP@MOF (SEM of TCPC and TCPP and EDS information are presented in Supplementary Information, Section S2, Figures S1 and S2). From these analyses it can be inferred that the use of TCPC and TCPP affects the morphology of the particles, comparatively to UiO-66(Hf).

The FT-IR spectra (Figure S3, in Supplementary Information) of the MOFs, TCPC@MOF and TCPP@MOF revealed peak profiles much more like those of UiO-66(Hf) than of the corresponding chlorin (TCPC) and porphyrin (TCPP). The most significant peaks occur at 1700–1650 cm^{-1} (ν(C=O)), $\approx$1580 cm^{-1} (ν_{as}(COO$^-$)), $\approx$1400 cm^{-1} (ν_s(COO$^-$)), $\approx$1020 cm^{-1} (δ(C−H)$_{ar}$) and $\approx$750 cm^{-1} (δ(C=C)). In particular, the weaker peaks corresponding to ν(C=O), observed in TCPC@MOF and TCPP@MOF in comparison with UiO-66(Hf), could be evidence of the coordination between the hexa-hafnium nodes and the porphyrin derivatives.
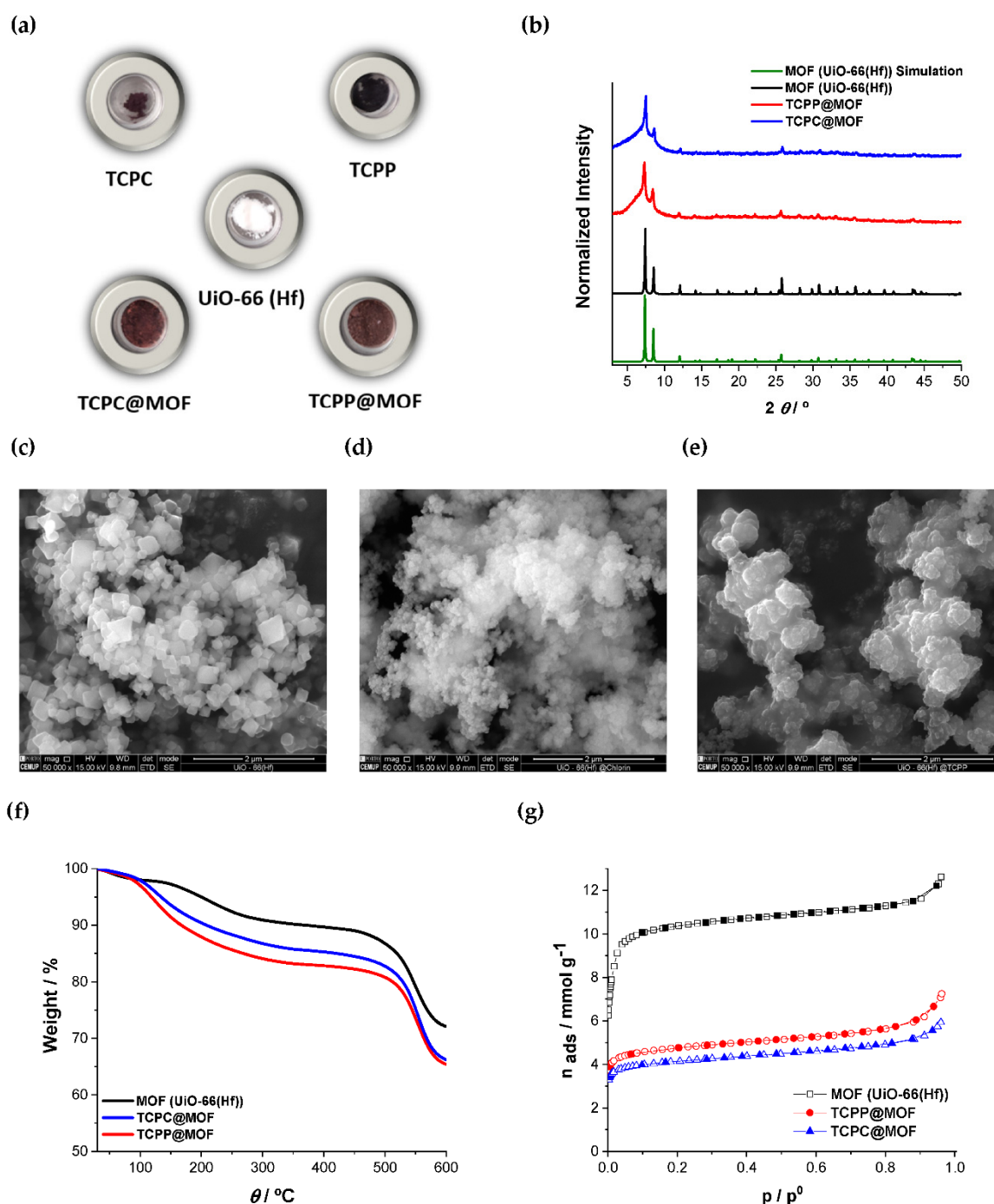
Figure 2. (**a**) Photographs of the prepared ligands (TCPC and TCPP) and MOFs (UiO-66(Hf), TCPP@MOF and TCPC@MOF), in the powder form; (**b**) PXRD patterns for MOF (UiO-66(Hf)) simulated structure [82] and for the prepared MOFs: UiO-66(Hf), TCPC@MOF and TCPP@MOF prepared by one-pot solvothermal reaction; (**c**–**e**) SEM images of UiO-66(Hf), TCPC@MOF and TCPP@MOF, respectively (50,000 × ampliation); (**f**) TGA of UiO-66(Hf) (black), TCPC@MOF (blue) and TCPP@MOF (red) from 30 to 600 °C performed with a heating rate of 5 °C/min in a 200 cm^3/min N$_2$ flow stream; and (**g**) N$_2$ adsorption-desorption isotherms determined at −196 °C for UiO-66(Hf), TCPC@MOF and TCPP@MOF (empty and filled symbols correspond to adsorption and desorption, respectively).

The ζ (zeta potential) of the MOFs can give us some relevant information relative to their surface functionalization. The differences observed in the ζ values, in milli-Q water and ethanol, between UiO-66(Hf), TCPC@MOF and TCPP@MOF, show that UiO-66(Hf)

surface is clearly changed in the presence of the TCPC and TCPP, particularly in ethanol (Table S1 in Supplementary Information).

A simple way to confirm the presence of TCPC and TCPP in the UiO-66(Hf) materials is through the study of their optical properties (the results in ethanol are summarized in Table S2 and Figure S4 in Supplementary Information). TCPC and TCPP reveal the expected Soret band and the four Q bands. The main difference between these two ligands occurs at the latter band region (639 < λ < 649 nm), where TCPC absorbs about 25 times more light (ε~1.14×10^5) than TCPP (ε~4.55×10^3). The UV-Vis spectra of UiO-66(Hf) dispersed in ethanol, show the typical continuous rise of dispersions as the wavelength decreases where an absorption band at approximately 265 nm can also be inferred as corresponding to the absorption of the benzene ring of the BDC ligand where no emission band is observed. On the other hand, TCPC@MOF and TCPP@MOF present the corresponding Soret and Q bands associated to TCPC and TCPP (Figure S4 in Supplementary Information), although they are red-shifted in comparison to the bands of the corresponding ligands (Table S2 in Supplementary Information). The main emission peak of the pyrrolidine-fused chlorin and porphyrin compounds and corresponding MOFs is around 649–660 nm followed by a lesser intense peak centered around 715–719 nm. Noteworthily, the PL spectra of TCPC and TCPP are similar to the corresponding loaded MOFs. The emission intensity of TCPC in ethanol is five-fold higher than the one corresponding to TCPP; while in the MOFs (TCPC@MOF and TCPP@MOF), the difference diminishes to less than two-fold higher.

The emission spectra comparison between TCPC/TCPP and the corresponding MOFs (TCPC@MOF and TCPP@MOF) shows: (i) a shift in the $\lambda_{em\,max}$; and (ii) an increase in the intensity of the longest wavelength emission band, particularly for TCPC@MOF. These changes can be correlated with a certain degree of aggregation of the porphyrinic-derivatives, a phenomenon observed both in solution and in solid matrices [83–85]. Nevertheless, these spectral features are typical of porphyrin-incorporated MOFs [86] and do not influence the materials' emission properties as fluorescent sensors. The results clearly show that the MOFs present the interesting photophysical characteristics of the chlorin and porphyrin derivatives used.

The thermogravimetric analysis (TGA) of the MOFs revealed mass change profiles similar to those previously reported for UiO-66(Hf) [79,80] (Figure 2f; the TGA related to TCPC and TCPP is presented at Figure S5 in Supplementary Information). A decomposition temperature of approximately 470 °C can be determined for all materials, a value close to other reports on UiO-66(Hf) [80,87], suggesting that the materials thermal properties are highly dependent of the UiO-66(Hf) framework.

The N_2 adsorption-desorption isotherms determined at −196 °C are illustrated in Figure 2g, and the values of volume adsorbed at 0.95 p° and apparent specific surface area resulting from the analysis of the adsorption by the BET method, using criteria recommended by Rouquerol et al. [88] and subsequently endorsed by IUPAC [89], are shown in Table 1. All the isotherms are type I of the IUPAC classification, which is characteristic of microporous UiO-66 architectures. Nevertheless, the adsorption isotherms of TCPC@MOF and TCPP@MOF are type I(a) of the IUPAC classification indicating that the materials have mainly narrow micropores, while UiO-66(Hf) has narrow and wider micropores as inferred from the type I(b) presented in Figure 2g. The BET area obtained for UiO-66(Hf) is in close proximity to reported values [87,90], while the incorporation of either TCPC or TCPP led to reduction in the BET area and microporosity. These observations suggest that part of the microporosity is closed, probably due to the incorporation of the chlorin or porphyrin, and/or that the bulky TCPC and TCPP ligands are partially occupying the space inside the pores. Consequently, micropores become narrower and less space is available for nitrogen adsorption. It can be noted that the differences between TCPC@MOF and TCPP@MOF are not very significant, but the reduction of the BET area and adsorbed N_2 volume is slightly larger in the first, possibly relating to the higher bulkiness of TCPC.

Table 1. BET area (A_{BET}) and adsorbed N_2 volume for UiO-66(Hf), TCPC@MOF and TCPP@MOF.

Material	$A_{BET}/m^2\ g^{-1}$	$V_{ads}\ (0.95\ p^o)/cm^3\ g^{-1}$
UiO-66(Hf)	940	0.43
TCPC@MOF	361	0.20
TCPP@MOF	414	0.24

3.2. MOF-Based Membranes

Considering our interest in MOF-based films toward the development of optical sensor devices [65–68] and the various promising applications of thin porous MOF films [91,92], we proceeded to the incorporation of TCPC@MOF and TCPP@MOF materials in PDMS polymeric membranes. The SEM images of a cross-section of the TCPC@MOF@PDMS based films (Figure 3a) reveal a constant thickness of 60 µm for the obtained membranes. Figure 3b also shows the flexibility of the polymer-based films and confirms that the MOF particles are totally embedded into the porous PDMS. Similar results were obtained for the TCPP@MOF@PDMS.
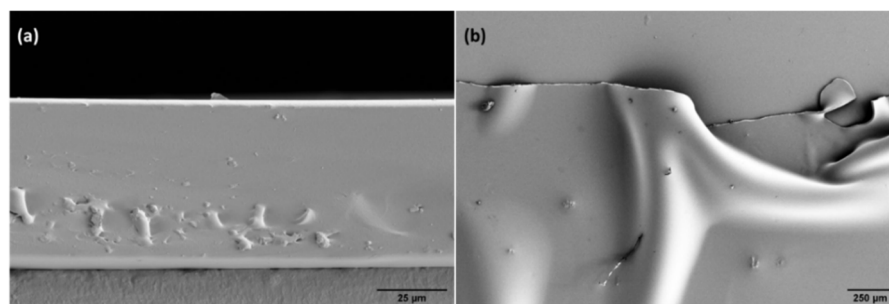
Figure 3. SEM images of (**a**) cross-section and (**b**) top view of TCPC@MOF@PDMS films.

The crystallinity of the TCPC@MOF and TCPP@MOF, once embedded in the PDMS membrane, was confirmed by XRD as shown in Figure 4. As can be observed, the diffractograms of both TCPC@MOF@PDMS and TCPP@MOF@PDMS reveals that the MOF particles are still crystalline after being processed into the PDMS membranes. In particular, the two main peaks of UiO-66(Hf) at 7.3° and 8.5° (2θ) can be clearly distinguished (highlighted in pale green color) from the noise signal produced by our diffractometer when analysing the mainly amorphous PDMS-based films. Other less intense peaks of the UiO-66 material can also be recognized at higher angles along with an amorphous phase around 12° (highlighted in pale pink color) corresponding to the polymeric matrix. It is noted that the membranes were not measured with a grazing incidence X-ray beam (GIXRD) because the signal coming from the amorphous phase (PDMS matrix) would be enhanced, thus masking the peaks from the crystalline MOF.

The fluorescence amplitude-average lifetime values from TCPC, TCPP, and TCPC(TCPP)@MOFs dispersed in the membrane are shown in Table 2, (PL decay curves and fits are shown in supporting information, Figure S6). The increase in PL lifetime, upon inclusion of TCPC and TCPP in UiO-66(Hf), is remarkable: a five-fold (nine-fold) lifetime increase is found when comparing TCPC@MOF (TCPP@MOF) with TCPC (TCPP). This observation underpins how porphyrin inclusion in UiO66(Hf) contributes to boosting the PL efficiency of the included chlorin and porphyrin compounds.
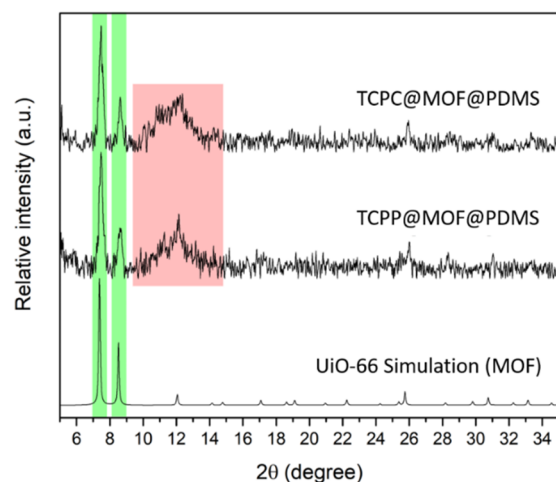
Figure 4. XRD diffractograms of UiO-66 simulated, TCPC@MOF@PDMS and TCPP@MOF@PDMS.

Table 2. PL lifetime and values obtained for TCPC, TCPP, UiO-66(Hf), TCPC@MOF and TCPP@MOF using the materials-embedded membranes.

Material	τ_{av}/ns	χ^2
TCPC	0.11	1.388
TCPP	0.12	1.066
UiO-66(Hf)	2.00	0.872
TCPC@MOF	0.55	1.111
TCPP@MOF	1.03	0.884

Figure 5 shows the absorption (black solid lines) and emission (λ_{exc} = 415 nm, red solid lines) spectra of TCPP@MOF@PDMS (a) and TCPC@MOF@PDMS (b) films. The corresponding spectra for pristine TCPC and TCPP in ethanol solution (dashed lines) are also shown for comparison purposes. As can be seen, the absorption spectra of the films show significant differences with respect to those in solution for TCPC and TCPP. Although the typical Soret and Q bands of the porphyrinic-based molecules are clearly distinguished in the spectra of the films, the large offsets seen in the spectra are ascribed to scattering produced by the MOF particles embedded into the PDMS films. Also, as stated previously, the main bands of the TCPC and TCPP molecules in solution are red-shifted when incorporated into the UiO-66 material and subsequently processed into the PDMS films. This phenomenon can be attributed to π-π stacking of the conjugated rings of TCPC and TCPP after their incorporation in the MOF. On the other hand, the fluorescence spectra of both films are similar to those of pure TCPC and TCPP in solution, demonstrating that the emission profile of the macrocyclic molecules remains almost unaltered after being incorporated into the non-emissive MOF particle embedded into the PDMS films. Moreover, a comparison of the emission intensities of the different films (Figure S7 in Supplementary Information) reveals that TCPC@MOF@PDMS exhibit 2.5 times more fluorescence than TCPP@MOF@PDMS. This higher fluorescence comes from the more emissive TCPC molecules compared to TCPP, as stated previously (Figure S4 in Supplementary Information). We then took advantage of these improved emission properties of the chlorin molecules for their application as more sensitive optical sensors using TCPC@MOF@PDMS films.
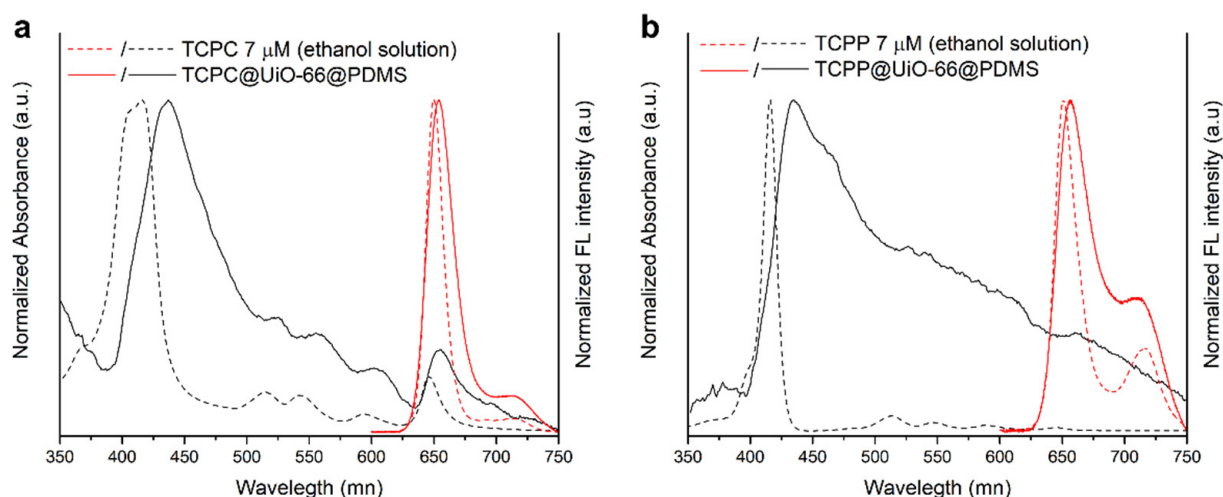
Figure 5. Absorbance (black lines) and FL emission (red lines) spectra of (**a**) TCPC@MOF@PDMS and (**b**) TCPP@MOF@PDMS films (solid lines) and the corresponding spectra of (**a**) TCPC and (**b**) TCPP in ethanol solution (dashed lines).

3.3. NO$_2$ Sensing Assays

TCPC@MOF@PDMS films were exposed to different concentrations of NO$_2$ gas, i.e., 500, 350, 250, 100, 50, 5, and 0.5 ppm, and their absorption and emission spectra were recorded. As shown in Figure 6a, exposure to increasing concentrations of the toxic gas resulted in a progressive red shift of the TCPC Soret band while a change in the number and position of the Q bands could also be inferred in the absorption spectra. These changes are compatible with a charge transfer between the electron-rich system of the chlorin and the strongly oxidizing NO$_2$, as previously reported for several free-base porphyrins [93–98]. However, a more sensitive sensing signal can be obtained in this case by following the emission changes as depicted in Figure 6b. As can be seen, a strong and progressive fluorescence quenching is observed when the TCPC@MOF@PDMS films were exposed to relatively low and increasing concentrations of NO$_2$. In particular, 500 ppm of the toxic gas produced a 96% quenching of the original emission of the complex film. Despite these high spectral changes, the recovery of the system was not possible after heating the sample or exposing it to a dry N$_2$ flow (data not shown), probably due to a covalent interaction between the NO$_2$ molecules and the product from the TCPC oxidation [99]. Other recovery strategies are in progress and deserve further research.
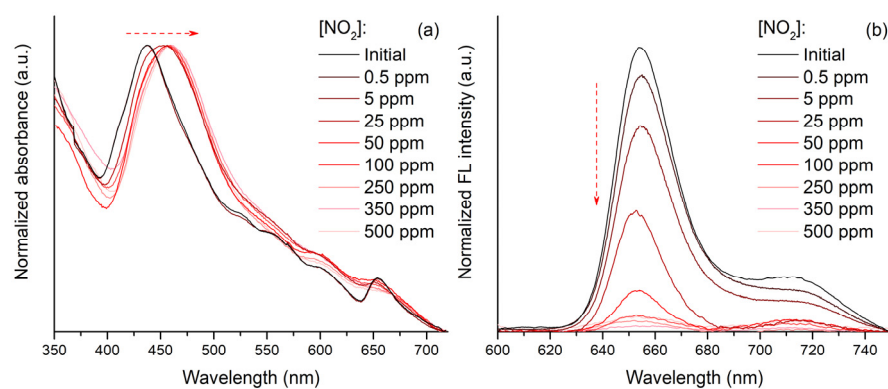
Figure 6. (**a**) Absorbance and (**b**) fluorescence (λ_{exc} = 415 nm) spectra of TCPC@MOF@PDMS films exposed to different NO$_2$ concentrations.

The fluorescent decay (quenching) in the presence of different concentrations of NO$_2$ was quantified as $\Phi = 1 − I/I_0$, where I_0 and I are the FL intensity at the wavelength of maximum emission (650 nm) before and after NO$_2$ exposure, respectively [93,100,101].

Figure 7 shows the fraction of the fluorescence quenching Φ as a function of the NO_2 concentration. The sensor exhibits a high response change at low concentrations of NO_2 (0–50 ppm). However, a saturation is observed when it is exposed to concentrations above 50 ppm, reaching a maximum response ($\Phi \times 100$) of >96%. Quenching-based fluorescent sensors in solution usually follow the Stern-Volmer model, where I_0/I follow a linear dependence with the analyte concentration [102]. However, a multi-site model is a better approximation for fluorescence-based gas sensors that do not follow the expected linear dependence [65,67,103,104]. In the two-site Stern-Volmer model, it is assumed that the sensor possesses at least two different binding sites, with their respective Stern-Volmer constants [65,105]. The equation of this model as a function of Φ can be written as:

$$\Phi = 1 - \frac{f_1}{1 + K1_1^{sv}[Q]} - \frac{f_2}{1 + K1_2^{sv}[Q]} \tag{1}$$

where f_1 and f_2 are the fractions of sites 1 and 2, respectively, where $f_1 + f_2 = 1$, $K1_1^{sv}$ and $K1_2^{sv}$ are the Stern-Volmer constants for each site, and [Q] is the quencher concentration; in our case, NO_2. Using this model, the experimental results showed a good fitting ($R^2 = 0.9837$) as can be seen in Figure 7. This good agreement with the experimental data could be explained in terms of the structural heterogeneity of the film where the TCPC sensing molecules must be occluded into the MOF cavities. This means that, in contrast to solution, the accessibility of the NO_2 molecules to the binding sites depends on many factors like their specific distribution, or the crystal shape and size. More particularly, the numerical fitting values of the proposed model for f_1 and f_2 were 0.9 and 0.1 respectively, and their corresponding Stern-Volmer constants were 0.098 and 24 ppm^{-1}. This means that around 90% of the available sites are less accessible, resulting in a lower binding energy, and therefore only occupied at high NO_2 concentrations.
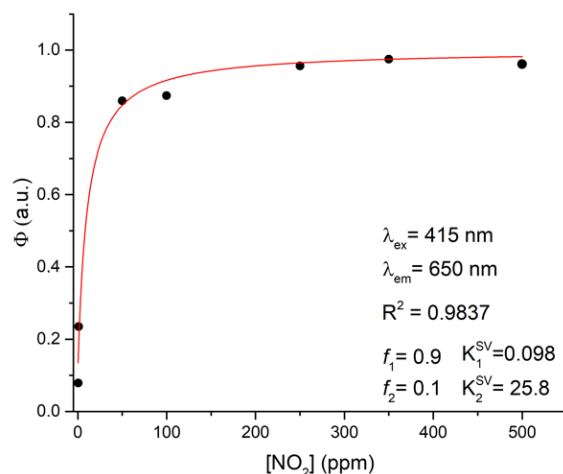
Figure 7. Quenching values Φ of the TCPC@MOF@PDMS film emission vs. NO_2 concentration and their fitting to the two-site Stern-Volmer model (see text for details).

Finally, the speed of the response was analysed by monitoring the temporal evolution of the FL emission intensity changes ($\Phi \times 100$) at different NO_2 concentrations as shown in Figure 8a. The corresponding spectra are shown in Figure S8 in Supplementary Information. As can be seen, the kinetic curves are characterized by a fast increasing of the quenching, followed by a stabilization of the curve until a complete saturation is reached. To evaluate the speed of response we used the t_{50} parameter, calculated as the time taken for the FL decay to reach 50% of its maximum change. Figure 8b shows the dependence of the t_{50} values with the gas concentration. As expected, the t_{50} decreases with the $[NO_2]$, showing that a few minutes are enough to obtain a measurable signal even for low analyte concentrations.
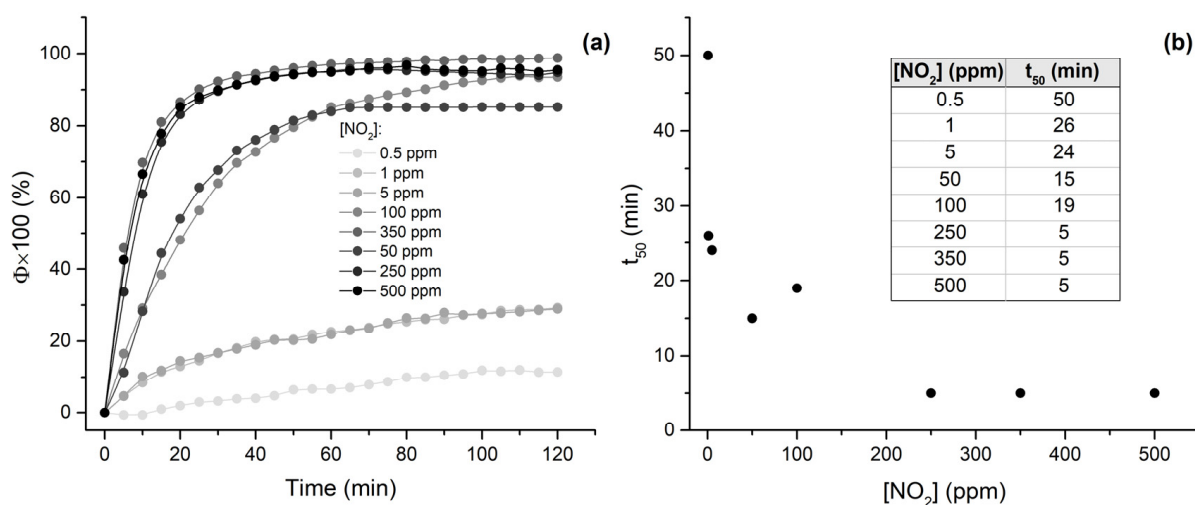
Figure 8. (**a**) Kinetic response of TCPC@MOF@PDMS under exposure to 0.5–500 ppm NO_2 gas and (**b**) the corresponding t_{50} values for this analyte concentration range.

4. Conclusions

In summary, a pyrrolidine-fused chlorin derivative (TCPC) was successfully incorporated into an MOF framework (UiO-66(Hf)) using a one-pot solvothermal synthesis. The material characterization indicates that the interesting photophysical properties of the chlorin derivative, even with a very small amount incorporated. were impressed in the framework and that the structural and stability features of the framework are maintained in the final material (TCPC@MOF). The composite was later embedded into a PDMS matrix and used in NO_2 sensing. Notably, despite the very low amount of chlorin incorporated in the MOF framework, the sensing experiments reveal that the composite responds to NO_2 in a range between 0 and 500 ppm, observing a 96% reduction of the original emission of the complex film for 500 ppm (t_{50} = 5 min). This work uncovers a new series of potential applications for chlorin derivatives usually associated to PDT applications, namely as optical gas sensors based on fluorescence properties.

References

1. Briefing: Europe's Air Quality Status. 2021. Available online: https://www.eea.europa.eu/publications/air-quality-status-2021 (accessed on 12 October 2021).
2. Meulenbelt, J. Nitrogen and nitrogen oxides. *Medicine* **2007**, *35*, 638. [CrossRef]
3. Curtis, L. PM2.5, NO_2, wildfires, and other environmental exposures are linked to higher Covid 19 incidence, severity, and death rates. *Environ. Sci. Pollut. Res.* **2021**, *28*, 54429–54447. [CrossRef] [PubMed]
4. Agency, E.E. Air Quality in Europe—2020 Report. Available online: https://www.eea.europa.eu/publications/air-quality-in-europe-2020-report (accessed on 12 October 2021).
5. Gutmacher, D.; Hoefer, U.; Wöllenstein, J. Gas sensor technologies for fire detection. *Sens. Actuators B Chem.* **2012**, *175*, 40–45. [CrossRef]
6. Schmitt, K.; Tarantik, K.; Pannek, C.; Wöllenstein, J. Colorimetric Materials for Fire Gas Detection—A Review. *Chemosensors* **2018**, *6*, 14. [CrossRef]
7. Korotcenkov, G. Properties, Advantages and Shortcomings for Applications Volume 1: Conventional Approaches. In *Handbook of Gas Sensor Materials*; Korotcenkov, G., Ed.; Springer-Verlag New York: New York, NY, USA, 2013; Volume 1.
8. Ma, Y.; Han, X.; Xu, S.; Wang, Z.; Li, W.; da Silva, I.; Chansai, S.; Lee, D.; Zou, Y.; Nikiel, M.; et al. Atomically Dispersed Copper Sites in a Metal–Organic Framework for Reduction of Nitrogen Dioxide. *J. Am. Chem. Soc.* **2021**, *143*, 10977–10985. [CrossRef]
9. Martínez-Ahumada, E.; Díaz-Ramírez, M.L.; Velásquez-Hernández, M.d.J.; Jancik, V.; Ibarra, I.A. Capture of toxic gases in MOFs: SO_2, H_2S, NH_3 and NOx. *Chem. Sci.* **2021**, *12*, 6772–6799. [CrossRef]
10. Islamoglu, T.; Chen, Z.; Wasson, M.C.; Buru, C.T.; Kirlikovali, K.O.; Afrin, U.; Mian, M.R.; Farha, O.K. Metal–Organic Frameworks against Toxic Chemicals. *Chem. Rev.* **2020**, *120*, 8130–8160. [CrossRef]
11. Liu, Y.; Howarth, A.J.; Hupp, J.T.; Farha, O.K. Selective Photooxidation of a Mustard-Gas Simulant Catalyzed by a Porphyrinic Metal–Organic Framework. *Angew. Chem. Int. Ed.* **2015**, *54*, 9001–9005. [CrossRef]
12. DeCoste, J.B.; Peterson, G.W. Metal–Organic Frameworks for Air Purification of Toxic Chemicals. *Chem. Rev.* **2014**, *114*, 5695–5727. [CrossRef]
13. Barea, E.; Montoro, C.; Navarro, J.A.R. Toxic gas removal—Metal–organic frameworks for the capture and degradation of toxic gases and vapours. *Chem. Soc. Rev.* **2014**, *43*, 5419–5430. [CrossRef]

14. Feng, Y.; Wang, Y.; Ying, Y. Structural design of metal–organic frameworks with tunable colorimetric responses for visual sensing applications. *Coord. Chem. Rev.* **2021**, *446*, 214102. [CrossRef]

15. Pamei, M.; Puzari, A. Luminescent transition metal–organic frameworks: An emerging sensor for detecting biologically essential metal ions. *Nano-Struct. Nano-Objects* **2019**, *19*, 100364. [CrossRef]

16. Dolgopolova, E.A.; Rice, A.M.; Martin, C.R.; Shustova, N.B. Photochemistry and photophysics of MOFs: Steps towards MOF-based sensing enhancements. *Chem. Soc. Rev.* **2018**, *47*, 4710–4728. [CrossRef] [PubMed]

17. Lustig, W.P.; Mukherjee, S.; Rudd, N.D.; Desai, A.V.; Li, J.; Ghosh, S.K. Metal–organic frameworks: Functional luminescent and photonic materials for sensing applications. *Chem. Soc. Rev.* **2017**, *46*, 3242–3285. [CrossRef]

18. Cui, Y.; Li, B.; He, H.; Zhou, W.; Chen, B.; Qian, G. Metal–Organic Frameworks as Platforms for Functional Materials. *Acc. Chem. Res.* **2016**, *49*, 483–493. [CrossRef]

19. Hu, Z.; Deibert, B.J.; Li, J. Luminescent metal–organic frameworks for chemical sensing and explosive detection. *Chem. Soc. Rev.* **2014**, *43*, 5815–5840. [CrossRef]

20. Cui, Y.; Yue, Y.; Qian, G.; Chen, B. Luminescent Functional Metal–Organic Frameworks. *Chem. Rev.* **2012**, *112*, 1126–1162. [CrossRef]

21. Gamonal, A.; Sun, C.; Mariano, A.L.; Fernandez-Bartolome, E.; Guerrero-SanVicente, E.; Vlaisavljevich, B.; Castells-Gil, J.; Marti-Gastaldo, C.; Poloni, R.; Wannemacher, R.; et al. Divergent Adsorption-Dependent Luminescence of Amino-Functionalized Lanthanide Metal–Organic Frameworks for Highly Sensitive NO_2 Sensors. *J. Phys. Chem. Lett.* **2020**, *11*, 3362–3368. [CrossRef]

22. Lian, X.; Fang, Y.; Joseph, E.; Wang, Q.; Li, J.; Banerjee, S.; Lollar, C.; Wang, X.; Zhou, H.-C. Enzyme–MOF (metal–organic framework) composites. *Chem. Soc. Rev.* **2017**, *46*, 3386–3401. [CrossRef]

23. Nath, I.; Chakraborty, J.; Verpoort, F. Metal organic frameworks mimicking natural enzymes: A structural and functional analogy. *Chem. Soc. Rev.* **2016**, *45*, 4127–4170. [CrossRef]

24. Wang, Q.; Astruc, D. State of the Art and Prospects in Metal–Organic Framework (MOF)-Based and MOF-Derived Nanocatalysis. *Chem. Rev.* **2020**, *120*, 1438–1511. [CrossRef]

25. Lee, J.; Farha, O.K.; Roberts, J.; Scheidt, K.A.; Nguyen, S.T.; Hupp, J.T. Metal–organic framework materials as catalysts. *Chem. Soc. Rev.* **2009**, *38*, 1450–1459. [CrossRef]

26. Jakobsen, S.; Gianolio, D.; Wragg, D.S.; Nilsen, M.H.; Emerich, H.; Bordiga, S.; Lamberti, C.; Olsbye, U.; Tilset, M.; Lillerud, K.P. Structural determination of a highly stable metal-organic framework with possible application to interim radioactive waste scavenging: Hf-UiO-66. *Phys. Rev. B* **2012**, *86*, 125429. [CrossRef]

27. Hu, Z.; Wang, Y.; Zhao, D. The chemistry and applications of hafnium and cerium(iv) metal–organic frameworks. *Chem. Soc. Rev.* **2021**, *50*, 4629–4683. [CrossRef] [PubMed]

28. Pal, S.; Yu, S.-S.; Kung, C.-W. Group 4 Metal-Based Metal—Organic Frameworks for Chemical Sensors. *Chemosensors* **2021**, *9*, 306. [CrossRef]

29. deKrafft, K.E.; Boyle, W.S.; Burk, L.M.; Zhou, O.Z.; Lin, W. Zr- and Hf-based nanoscale metal–organic frameworks as contrast agents for computed tomography. *J. Mater. Chem.* **2012**, *22*, 18139–18144. [CrossRef]

30. Nandi, S.; Biswas, S. A diamino functionalized metal-organic framework for fluorometric recognition of free chlorine in environmental water samples. *Microporous Mesoporous Mater.* **2020**, *299*, 110116. [CrossRef]

31. Dalapati, R.; Biswas, S. A Pyrene-Functionalized Metal–Organic Framework for Nonenzymatic and Ratiometric Detection of Uric Acid in Biological Fluid via Conformational Change. *Inorg. Chem.* **2019**, *58*, 5654–5663. [CrossRef]

32. Sk, M.; Nandi, S.; Singh, R.K.; Trivedi, V.; Biswas, S. Selective Sensing of Peroxynitrite by Hf-Based UiO-66-B(OH)$_2$ Metal–Organic Framework: Applicability to Cell Imaging. *Inorg. Chem.* **2018**, *57*, 10128–10136. [CrossRef]

33. Shahat, A.; Hassan, H.M.A.; Azzazy, H.M.E. Optical metal-organic framework sensor for selective discrimination of some toxic metal ions in water. *Anal. Chim. Acta* **2013**, *793*, 90–98. [CrossRef]

34. Xu, X.-Y.; Yan, B. Eu(III) functionalized Zr-based metal-organic framework as excellent fluorescent probe for Cd^{2+} detection in aqueous environment. *Sens. Actuators B Chem.* **2016**, *222*, 347–353. [CrossRef]

35. Yang, Y.; Liu, X.; Yan, D.; Deng, P.; Guo, Z.; Zhan, H. Europium ion post-functionalized zirconium metal–organic frameworks as luminescent probes for effectively sensing hydrazine hydrate. *RSC Adv.* **2018**, *8*, 17471–17476. [CrossRef] [PubMed]

36. Xiaoxiong, Z.; Wenjun, Z.; Cuiliu, L.; Xiaohong, Q.; Chengyu, Z. Eu^{3+}-Postdoped UIO-66-Type Metal–Organic Framework as a Luminescent Sensor for Hg^{2+} Detection in Aqueous Media. *Inorg. Chem.* **2019**, *58*, 3910–3915. [CrossRef] [PubMed]

37. Zhao, X.; Wang, Y.; Hao, X.; Liu, W. Fluorescent molecule incorporated metal-organic framework for fluoride sensing in aqueous solution. *Appl. Surf. Sci.* **2017**, *402*, 129–135. [CrossRef]

38. Govindaraju, S.; Puthiaraj, P.; Lee, M.-H.; Yun, K. Photoluminescent AuNCs@UiO-66 for Ultrasensitive Detection of Mercury in Water Samples. *ACS Omega* **2018**, *3*, 12052–12059. [CrossRef]

39. Liu, L.; Zhou, Y.; Liu, S.; Xu, M. The Applications of Metal−Organic Frameworks in Electrochemical Sensors. *ChemElectroChem* **2018**, *5*, 6–19. [CrossRef]

40. Diamantis, S.A.; Margariti, A.; Pournara, A.D.; Papaefstathiou, G.S.; Manos, M.J.; Lazarides, T. Luminescent metal–organic frameworks as chemical sensors: Common pitfalls and proposed best practices. *Inorg. Chem. Front.* **2018**, *5*, 1493–1511. [CrossRef]

41. Zhang, Y.; Yuan, S.; Day, G.; Wang, X.; Yang, X.; Zhou, H.-C. Luminescent sensors based on metal-organic frameworks. *Coord. Chem. Rev.* **2018**, *354*, 28–45. [CrossRef]

42. Li, H.-Y.; Zhao, S.-N.; Zang, S.-Q.; Li, J. Functional metal–organic frameworks as effective sensors of gases and volatile compounds. *Chem. Soc. Rev.* **2020**, *49*, 6364–6401. [CrossRef]

43. Melnikov, P.; Bobrov, A.; Marfin, Y. On the Use of Polymer-Based Composites for the Creation of Optical Sensors: A Review. *Polymers* **2022**, *14*, 4448. [CrossRef] [PubMed]

44. Huh, S.; Kim, S.-J.; Kim, Y. Porphyrinic metal–organic frameworks from custom-designed porphyrins. *CrystEngComm* **2016**, *18*, 345–368. [CrossRef]

45. Yu, W.; Zhen, W.; Zhang, Q.; Li, Y.; Luo, H.; He, J.; Liu, Y. Porphyrin-Based Metal−Organic Framework Compounds as Promising Nanomedicines in Photodynamic Therapy. *ChemMedChem* **2020**, *15*, 1766–1775. [CrossRef]

46. Horcajada, P.; Chalati, T.; Serre, C.; Gillet, B.; Sebrie, C.; Baati, T.; Eubank, J.F.; Heurtaux, D.; Clayette, P.; Kreuz, C.; et al. Porous metal–organic-framework nanoscale carriers as a potential platform for drug delivery and imaging. *Nat. Mater.* **2010**, *9*, 172–178. [CrossRef]

47. Cai, H.; Huang, Y.-L.; Li, D. Biological metal–organic frameworks: Structures, host–guest chemistry and bio-applications. *Coord. Chem. Rev.* **2019**, *378*, 207–221. [CrossRef]

48. Morozova, S.M.; Sharsheeva, A.; Morozov, M.I.; Vinogradov, A.V.; Hey-Hawkins, E. Bioresponsive metal–organic frameworks: Rational design and function. *Coord. Chem. Rev.* **2021**, *431*, 213682. [CrossRef]

49. Fu, X.; Yang, Z.; Deng, T.; Chen, J.; Wen, Y.; Fu, X.; Zhou, L.; Zhu, Z.; Yu, C. A natural polysaccharide mediated MOF-based Ce6 delivery system with improved biological properties for photodynamic therapy. *J. Mater. Chem. B* **2020**, *8*, 1481–1488. [CrossRef] [PubMed]

50. Wang, H.; Chen, Y.; Wang, H.; Liu, X.; Zhou, X.; Wang, F. DNAzyme-Loaded Metal–Organic Frameworks (MOFs) for Self-Sufficient Gene Therapy. *Angew. Chem. Int. Ed.* **2019**, *58*, 7380–7384. [CrossRef] [PubMed]

51. Ding, L.; Lin, X.; Lin, Z.; Wu, Y.; Liu, X.; Liu, J.; Wu, M.; Zhang, X.; Zeng, Y. Cancer Cell-Targeted Photosensitizer and Therapeutic Protein Co-Delivery Nanoplatform Based on a Metal–Organic Framework for Enhanced Synergistic Photodynamic and Protein Therapy. *ACS Appl. Mater. Interfaces* **2020**, *12*, 36906–36916. [CrossRef]

52. Sheng, S.; Liu, F.; Lin, L.; Yan, N.; Wang, Y.; Xu, C.; Tian, H.; Chen, X. Nanozyme-mediated cascade reaction based on metal-organic framework for synergetic chemo-photodynamic tumor therapy. *J. Control. Release* **2020**, *328*, 631–639. [CrossRef]

53. Calmeiro, J.M.D.; Dias, C.J.; Ramos, C.I.V.; Almeida, A.; Tomé, J.P.C.; Faustino, M.A.F.; Lourenço, L.M.O. Comparative photodynamic inactivation of bioluminescent E. coli by pyridinium and inverted pyridinium chlorins. *Dye. Pigment.* **2020**, *173*, 107410. [CrossRef]

54. Sobotta, L.; Sniechowska, J.; Ziental, D.; Dlugaszewska, J.; Potrzebowski, M.J. Chlorins with (trifluoromethyl)phenyl substituents— Synthesis, lipid formulation and photodynamic activity against bacteria. *Dye. Pigment.* **2019**, *160*, 292–300. [CrossRef]

55. Heredia, D.A.; Durantini, A.M.; Sarotti, A.M.; Gsponer, N.S.; Ferreyra, D.D.; Bertolotti, S.G.; Milanesio, M.E.; Durantini, E.N. Proton-Dependent Switching of a Novel Amino Chlorin Derivative as a Fluorescent Probe and Photosensitizer for Acidic Media. *Chem. A Eur. J.* **2018**, *24*, 5950–5961. [CrossRef]

56. Almeida, J.; Zhang, G.; Wang, M.; Queirós, C.; Cerqueira, A.F.R.; Tomé, A.C.; Barone, G.; Vicente, M.G.H.; Hey-Hawkins, E.; Silva, A.M.G.; et al. Synthesis, characterization, and cellular investigations of porphyrin– and chlorin–indomethacin conjugates for photodynamic therapy of cancer. *Org. Biomol. Chem.* **2021**, *19*, 6501–6512. [CrossRef] [PubMed]

57. Thompson, S.A.; Aggarwal, A.; Singh, S.; Adam, A.P.; Tome, J.P.C.; Drain, C.M. Compromising the plasma membrane as a secondary target in photodynamic therapy-induced necrosis. *Bioorganic Med. Chem.* **2018**, *26*, 5224–5228. [CrossRef]

58. Hirohara, S.; Oka, C.; Totani, M.; Obata, M.; Yuasa, J.; Ito, H.; Tamura, M.; Matsui, H.; Kakiuchi, K.; Kawai, T.; et al. Synthesis, Photophysical Properties, and Biological Evaluation of trans-Bisthioglycosylated Tetrakis(fluorophenyl)chlorin for Photodynamic Therapy. *J. Med. Chem.* **2015**, *58*, 8658–8670. [CrossRef] [PubMed]

59. Hao, E.; Friso, E.; Miotto, G.; Jori, G.; Soncin, M.; Fabris, C.; Sibrian-Vazquez, M.; Vicente, M.G.H. Synthesis and biological investigations of tetrakis(p-carboranylthio-tetrafluorophenyl)chlorin (TPFC). *Org. Biomol. Chem.* **2008**, *6*, 3732–3740. [CrossRef]

60. Castro, K.A.D.F.; Pires, S.M.G.; Ribeiro, M.A.; Simões, M.M.Q.; Neves, M.G.P.M.S.; Schreiner, W.H.; Wypych, F.; Cavaleiro, J.A.S.; Nakagaki, S. Manganese chlorins immobilized on silica as oxidation reaction catalysts. *J. Colloid Interface Sci.* **2015**, *450*, 339–352. [CrossRef]

61. Pires, S.M.G.; Paula, R.D.; Simões, M.M.Q.; Neves, M.G.P.M.S.; Santos, I.C.M.S.; Tomé, A.C.; Cavaleiro, J.A.S. A new silica-supported manganese chlorin as a biomimetic oxidation catalyst. *Catal. Commun.* **2009**, *11*, 24–28. [CrossRef]

62. Marui, K.; Nomoto, A.; Akashi, H.; Ogawa, A. Green Oxidation of Amines to Imines Based on the Development of Novel Catalytic Systems Using Molecular Oxygen or Hydrogen Peroxide. *Synthesis* **2016**, *48*, 31–42.

63. Guillén, M.G.; Gámez, F.; Suárez, B.; Queirós, C.; Silva, A.M.G.; Barranco, Á.; Sánchez-Valencia, J.R.; Pedrosa, J.M.; Lopes-Costa, T. Preparation and Optimization of Fluorescent Thin Films of Rosamine-SiO₂/TiO₂ Composites for NO₂ Sensing. *Materials* **2017**, *10*, 124. [CrossRef]

64. Guillén, M.G.; Suárez, B.; Roales, J.; Gámez, F.; Vargas, A.P.; Moscoso, F.G.; Lopes-Costa, T.; Queirós, C.; Silva, A.M.G.; Pedrosa, J.M. Fluorescent Rosamine/TiO₂ Composite Films for the Optical Detection of NO₂. *J. Sens.* **2018**, *2018*, 7954839. [CrossRef]

65. Moscoso, F.G.; Almeida, J.; Sousaraei, A.; Lopes-Costa, T.; Silva, A.M.G.; Cabanillas-Gonzalez, J.; Cunha-Silva, L.; Pedrosa, J.M. Luminescent MOF crystals embedded in PMMA/PDMS transparent films as effective NO₂ gas sensors. *Mol. Syst. Des. Eng.* **2020**, *5*, 1048–1056. [CrossRef]

66. Sousaraei, A.; Queirós, C.; Moscoso, F.G.; Silva, A.M.G.; Lopes-Costa, T.; Pedrosa, J.M.; Cunha-Silva, L.; Cabanillas-Gonzalez, J. Reversible Protonation of Porphyrinic Metal-Organic Frameworks Embedded in Nanoporous Polydimethylsiloxane for Colorimetric Sensing. *Adv. Mater. Interfaces* **2021**, *8*, 2001759. [CrossRef]

67. Moscoso, F.G.; Almeida, J.; Sousaraei, A.; Lopes-Costa, T.; Silva, A.M.G.; Cabanillas-Gonzalez, J.; Cunha-Silva, L.; Pedrosa, J.M. A lanthanide MOF immobilized in PMMA transparent films as a selective fluorescence sensor for nitroaromatic explosive vapours. *J. Mater. Chem. C* **2020**, *8*, 3626–3630. [CrossRef]

68. Sousaraei, A.; Queirós, C.; Moscoso, F.G.; Lopes-Costa, T.; Pedrosa, J.M.; Silva, A.M.G.; Cunha-Silva, L.; Cabanillas-Gonzalez, J. Subppm Amine Detection via Absorption and Luminescence Turn-On Caused by Ligand Exchange in Metal Organic Frameworks. *Anal. Chem.* **2019**, *91*, 15853–15859. [CrossRef] [PubMed]

69. Sakamaki, Y.; Ozdemir, J.; Heidrick, Z.; Azzun, A.; Watson, O.; Tsuji, M.; Salmon, C.; Sinha, A.; Batta-Mpouma, J.; McConnell, Z.; et al. A Bioconjugated Chlorin-Based Metal–Organic Framework for Targeted Photodynamic Therapy of Triple Negative Breast and Pancreatic Cancers. *ACS Appl. Bio Mater.* **2021**, *4*, 1432–1440. [CrossRef]

70. Vargas, A.P.; Almeida, J.; Gámez, F.; Roales, J.; Queirós, C.; Rangel, M.; Lopes-Costa, T.; Silva, A.M.G.; Pedrosa, J.M. Synthesis of a highly emissive carboxylated pyrrolidine-fused chlorin for optical sensing of TATP vapours. *Dye. Pigment.* **2021**, *195*, 109721. [CrossRef]

71. Wang, Y.; Liu, D.; Yin, J.; Shang, Y.; Du, J.; Kang, Z.; Wang, R.; Chen, Y.; Sun, D.; Jiang, J. An ultrafast responsive NO_2 gas sensor based on a hydrogen-bonded organic framework material. *Chem. Commun.* **2020**, *56*, 703–706. [CrossRef] [PubMed]

72. Tuerdi, G.; Yan, Y.; Yimit, A. Optical and electrochemical gas sensing applications of Cu Tetraphenylporphyrin thin films. *Optik* **2019**, *183*, 114–123. [CrossRef]

73. Zhu, P.; Song, F.; Ma, P.; Wang, Y.; Chen, C.; Feng, J. Morphology-controlled self-assembly of a ferrocene–porphyrin based NO_2 gas sensor: Tuning the semiconducting nature via solvent–solute interaction. *J. Mater. Chem. C* **2016**, *4*, 10471–10478. [CrossRef]

74. Su, H.C.; Tran, T.-T.; Bosze, W.; Myung, N.V. Chemiresistive sensor arrays for detection of air pollutants based on carbon nanotubes functionalized with porphyrin and phthalocyanine derivatives. *Sens. Actuators Rep.* **2020**, *2*, 100011. [CrossRef]

75. Wang, Y.; Ma, P.; Song, F.; Yao, S.; Chen, C.; Zhu, P. Comparative NO_2-sensing in cobalt and metal-free porphyrin nanotubes. *J. Colloid Interface Sci.* **2017**, *490*, 129–136. [CrossRef]

76. Lee, J.I.; Kim, M.; Park, K.C.; Lee, C.Y.; Park, Y.D. Polythiophene hybrid film with zirconium–porphyrin metal–organic framework for improved charge carrier transport and NO_2 gas sensing. *Mater. Chem. Phys.* **2022**, *278*, 125661. [CrossRef]

77. Zheng, X.; Wang, L.; Guan, Y.; Pei, Q.; Jiang, J.; Xie, Z. Integration of metal-organic framework with a photoactive porous-organic polymer for interface enhanced phototherapy. *Biomaterials* **2020**, *235*, 119792. [CrossRef]

78. Lu, K.; He, C.; Lin, W. A Chlorin-Based Nanoscale Metal-Organic Framework for Photodynamic Therapy of Colon Cancers. *J. Am. Chem. Soc.* **2015**, *137*, 7600–7603. [CrossRef]

79. Hu, Z.; Nalaparaju, A.; Peng, Y.; Jiang, J.; Zhao, D. Modulated Hydrothermal Synthesis of UiO-66(Hf)-Type Metal–Organic Frameworks for Optimal Carbon Dioxide Separation. *Inorg. Chem.* **2016**, *55*, 1134–1141. [CrossRef]

80. Zheng, X.; Wang, L.; Liu, M.; Lei, P.; Liu, F.; Xie, Z. Nanoscale Mixed-Component Metal–Organic Frameworks with Photosensitizer Spatial-Arrangement-Dependent Photochemistry for Multimodal-Imaging-Guided Photothermal Therapy. *Chem. Mater.* **2018**, *30*, 6867–6876. [CrossRef]

81. Liao, X.; Wang, X.; Wang, F.; Yao, Y.; Lu, S. Ligand Modified Metal Organic Framework UiO-66: A Highly Efficient and Stable Catalyst for Oxidative Desulfurization. *J. Inorg. Organomet. Polym. Mater.* **2021**, *31*, 756–762. [CrossRef]

82. Øien, S.; Wragg, D.; Reinsch, H.; Svelle, S.; Bordiga, S.; Lamberti, C.; Lillerud, K.P. Detailed Structure Analysis of Atomic Positions and Defects in Zirconium Metal–Organic Frameworks. *Cryst. Growth Des.* **2014**, *14*, 5370–5372. [CrossRef]

83. Melnikov, P.V.; Naumova, A.O.; Alexandrovskaya, A.Y.; Zaitsev, N.K. Optimizing Production Conditions for a Composite Optical Oxygen Sensor Using Mesoporous SiO2. *Nanotechnologies Russ.* **2018**, *13*, 602–608. [CrossRef]

84. Ghosh, M.; Nath, S.; Hajra, A.; Sinha, S. Fluorescence self-quenching of tetraphenylporphyrin in liquid medium. *J. Lumin.* **2013**, *141*, 87–92. [CrossRef]

85. Ni, M.; Gong, M.; Li, X.; Gu, J.; Li, B.; Chen, Y. Dimensions of fluorescence kinetic concentration of doped morphology homologs synthesized by TCPP and UiO-66 MOF. *Appl. Mater. Today* **2021**, *23*, 100982. [CrossRef]

86. Simon-Yarza, T.; Mielcarek, A.; Couvreur, P.; Serre, C. Nanoparticles of Metal-Organic Frameworks: On the Road to In Vivo Efficacy in Biomedicine. *Adv. Mater.* **2018**, *30*, 1707365. [CrossRef]

87. Dang, Y.T.; Hoang, H.T.; Dong, H.C.; Bui, K.-B.T.; Nguyen, L.H.T.; Phan, T.B.; Kawazoe, Y.; Doan, T.L.H. Microwave-assisted synthesis of nano Hf- and Zr-based metal-organic frameworks for enhancement of curcumin adsorption. *Microporous Mesoporous Mater.* **2020**, *298*, 110064. [CrossRef]

88. Rouquerol, J.; Rouquerol, F.; Sing, K. *Adsorption by Powders and Porous Solids*; Academic Press: London, UK, 1999.

89. Thommes, M.; Kaneko, K.; Neimark, A.V.; Olivier, J.P.; Rodriguez-Reinoso, F.; Rouquerol, J.; Sing, K.S.W. Physisorption of gases, with special reference to the evaluation of surface area and pore size distribution (IUPAC Technical Report). *Pure Appl. Chem.* **2015**, *87*, 1051–1069. [CrossRef]

90. Bakuru, V.R.; Churipard, S.R.; Maradur, S.P.; Kalidindi, S.B. Exploring the Brønsted acidity of UiO-66 (Zr, Ce, Hf) metal–organic frameworks for efficient solketal synthesis from glycerol acetalization. *Dalton Trans.* **2019**, *48*, 843–847. [CrossRef] [PubMed]

91. Crivello, C.; Sevim, S.; Graniel, O.; Franco, C.; Pané, S.; Puigmartí-Luis, J.; Muñoz-Rojas, D. Advanced technologies for the fabrication of MOF thin films. *Mater. Horiz.* **2021**, *8*, 168–178. [CrossRef]

92.　Shekhah, O.; Liu, J.; Fischer, R.A.; Wöll, C. MOF thin films: Existing and future applications. *Chem. Soc. Rev.* **2011**, *40*, 1081–1106. [CrossRef]

93.　Roales, J.; Pedrosa, J.M.; Guillén, M.G.; Lopes-Costa, T.; Castillero, P.; Barranco, A.; González-Elipe, A.R. Free-Base Carboxyphenyl Porphyrin Films Using a TiO$_2$ Columnar Matrix: Characterization and Application as NO$_2$ Sensors. *Sensors* **2015**, *15*, 11118–11132. [CrossRef]

94.　Richardson, T.H.; Dooling, C.M.; Jones, L.T.; Brook, R.A. Development and optimization of porphyrin gas sensing LB films. *Adv. Colloid Interface Sci.* **2005**, *116*, 81–96. [CrossRef]

95.　Pedrosa, J.M.; Dooling, C.M.; Richardson, T.H.; Hyde, R.K.; Hunter, C.A.; Martín, M.T.; Camacho, L. Influence of Molecular Organization of Asymmetrically Substituted Porphyrins on Their Response to NO$_2$ Gas. *Langmuir* **2002**, *18*, 7594–7601. [CrossRef]

96.　Gulino, A.; Mineo, P.; Scamporrino, E.; Vitalini, D.; Fragalà, I. Molecularly Engineered Silica Surfaces with an Assembled Porphyrin Monolayer as Optical NO$_2$ Molecular Recognizers. *Chem. Mater.* **2004**, *16*, 1838–1840. [CrossRef]

97.　Dooling, C.M.; Worsfold, O.; Richardson, T.H.; Tregonning, R.; Vysotsky, M.O.; Hunter, C.A.; Kato, K.; Shinbo, K.; Kaneko, F. Fast, reversible optical sensing of NO$_2$ using 5,10,15,20-tetrakis[3,4-bis(2-ethylhexyloxy)phenyl]-21H,23H-porphine assemblies. *J. Mater. Chem.* **2001**, *11*, 392–398. [CrossRef]

98.　Gulino, A.; Bazzano, S.; Mineo, P.; Scamporrino, E.; Vitalini, D.; Fragalà, I. Characterization, Optical Recognition Behavior, Sensitivity, and Selectivity of Silica Surfaces Functionalized with a Porphyrin Monolayer. *Chem. Mater.* **2005**, *17*, 521–526. [CrossRef]

99.　Abudukeremu, H.; Kari, N.; Zhang, Y.; Wang, J.; Nizamidin, P.; Abliz, S.; Yimit, A. Highly sensitive free-base-porphyrin-based thin-film optical waveguide sensor for detection of low concentration NO$_2$ gas at ambient temperature. *J. Mater. Sci.* **2018**, *53*, 10822–10834. [CrossRef]

100.　Zakavi, S.; Omidyan, R.; Ebrahimi, L.; Heidarizadi, F. Substitution effects on the UV–vis and 1H NMR spectra of the dications of meso and/or β substituted porphyrins with trifluoroacetic acid: Electron-deficient porphyrins compared to the electron-rich ones. *Inorg. Chem. Commun.* **2011**, *14*, 1827–1832. [CrossRef]

101.　Shen, Y.; Zhong, X.; Zhang, J.; Li, T.; Zhao, S.; Cui, B.; Wei, D.; Zhang, Y.; Wei, K. In-situ growth of mesoporous In2O3 nanorod arrays on a porous ceramic substrate for ppb-level NO$_2$ detection at room temperature. *Appl. Surf. Sci.* **2019**, *498*, 143873. [CrossRef]

102.　Lakowicz, J.R. *Principles of Fluorescence Spectroscopy*, 3rd ed.; Springer: Boston, MA, USA, 2006.

103.　Guillén, M.G.; Gámez, F.; Lopes-Costa, T.; Cabanillas-González, J.; Pedrosa, J.M. A fluorescence gas sensor based on Förster Resonance Energy Transfer between polyfluorene and bromocresol green assembled in thin films. *Sens. Actuators B Chem.* **2016**, *236*, 136–143. [CrossRef]

104.　Guillén, M.G.; Gámez, F.; Lopes-Costa, T.; Castro-Smirnov, J.R.; Wannemacher, R.; Cabanillas-González, J.; Pedrosa, J.M. Amplified spontaneous emission in action: Sub-ppm optical detection of acid vapors in poly[2-methoxy-5-(2-ethylhexyloxy)-1,4-phenylenevinylene] thin films. *Sens. Actuators B Chem.* **2018**, *255*, 1354–1361. [CrossRef]

105.　Demas, J.N.; DeGraff, B.A.; Xu, W. Modeling of Luminescence Quenching-Based Sensors: Comparison of Multisite and Nonlinear Gas Solubility Models. *Anal. Chem.* **1995**, *67*, 1377–1380. [CrossRef]